ACS OMEGA

http://pubs.acs.org/journal/acsodf

Article

Ab Initio Calculation of Surface Thermochemistry for Popular Solid Transition Metal-Based Species

Muhammad Fahad Arshad, Ling-Nan Wu, Achraf El Kasmi, Wu Qin, and Zhen-Yu Tian*

Cite This: *ACS Omega* 2021, 6, 22525−22536

Read Online

ACCESS | Metrics & More | Article Recommendations | Supporting Information

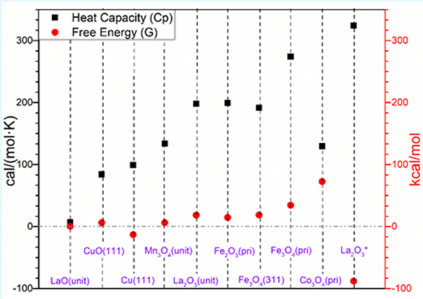

Heat capacity at constant pressure and free energy of transition metal-based species at 298 K.

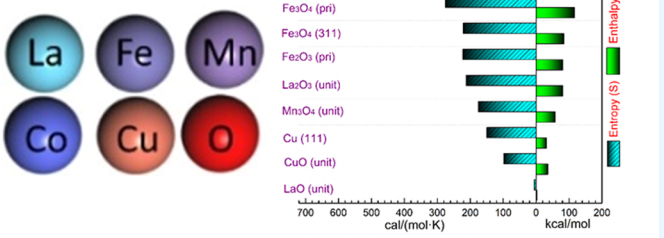

Entropy and enthalpy of transition metal-based species at 298 K.

ABSTRACT: This work reports the thermochemistry calculations for solid-phase periodic models of ten popular transition metal-based species. These model structures were refined to stable geometry by geometric optimization along with calculating the thermodynamic properties including enthalpy, entropy, heat capacity at constant pressure, and Gibbs free energy by DMol^3 package via first-principles ab initio calculations. The temperature-dependent thermochemistry values were converted to a NASA seven-polynomial format. The behavior of different thermodynamic parameters based on temperature was investigated and their comparative analysis was done. A higher number of atoms tends to show higher thermodynamic values. Moreover, these thermodynamic values agree reasonably well with previously reported experimental and computational values. Metal copper shows higher thermodynamic values as compared to its oxide. The thermodynamic properties of lanthanum-based oxides have been newly calculated through the ab initio method. Amorphous structures reveal higher thermodynamic values compared to their crystalline counterparts. A comparison between different transition metal-based species gives a better understanding of the different crystalline structures and their surface sites. These calculated thermodynamic data and polynomials can be used for a variety of thermodynamic calculations and kinetic modeling.

1. INTRODUCTION

The chemical kinetics and mechanisms of chemicals in their different phases have been studied for over a century, and their understanding was the foundation of our modern-day futuristic world. Equilibrium-phase modeling is one of the most important fundamental sciences for the development process in the chemical industry.[1] Thermodynamic data provide a model-based evaluation for the basis of a wide variety of processes including liquid−liquid extraction, solid-based heterogeneous catalysis, and distillation. It also provides a possibility to evaluate data through flow sheet simulations.[2]

Thermochemistry research and its related works were started over 130 years ago. The earliest one was performed by Mallard and Le Chatelier in 1883,[3] and then over the years, researchers have been working on, generating, and searching for the thermodynamic properties of old and new materials to better understand their behavior and kinetics.[4−10] Burcat[11,12] calculated the thermochemistry of materials using Gaussian03 G3/B3LYP (as known as G3B3) calculations. These results were calculated through geometric optimization using a nonperiodic model.[11] Transition metal-based species are composed of transition metals along with other species; they are abundantly present on earth and are used for a wide variety of applications, including catalytic reactions and photo-assisted adsorption−desorption. They are deeply studied from lab-scale developing research to industrial-scale applications.[13,14]

Previous thermodynamic calculations were mostly limited to gas-phase species with nonperiodic boundary conditions.[15] They were unable to precisely calculate species under their 3d periodic boundary conditions due to the multiple possibilities of order and arrangements that made the calculations more

Received: April 24, 2021
Accepted: July 21, 2021
Published: August 26, 2021

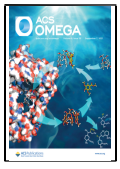

complicated. These multiple possibilities influence the species' thermophysical behavior. Some recent developments through quantum methods have been made in the field of material studies, including the usage of machine learning,[16,17] Paramendism algorithm,[18] and quasi-harmonic approximations,[19] which are still in the development phase. The present work is an extension toward the understanding of thermodynamic properties for the development of transition metals and their oxides. Understanding the transition metal-based surface and its thermodynamic properties is of immense importance toward the development of the modern chemical industry and environmental protection.[20] The method of simultaneous regression has been used for the approximate conversion of thermochemical properties into a polynomial format, which finally provides NASA's famous seven-term polynomial coefficients.[21,22] Polynomials allow us to simulate thermodynamic properties over a range of temperatures. This gives better insight into the chemical reactions taking place from a small experimental scale to an extraordinary industrial scale. The approach of generating polynomial fits used in the previous works[11] of two temperature ranges was implemented in this work. These calculations enable us to explore the properties of a material beyond its nonperiodic state with a higher number of atoms and layers, which enables us to calculate better and more accurate results compared to its predecessors. Meanwhile, a limitation of the density functional theory (DFT) calculation is that the exact functional of the Hohenberg−Kohn theorem is not known. Every time a DFT calculation is performed, there is an intrinsic uncertainty that exists between the true ground-state energies of the Schrodinger equation and those calculated through the DFT method. Another limitation lies in its computing capability, as a larger and more layered composition of materials might show better results, but these are limited to the modern generation of computational technology. A careful comparison with calorimetry-based experimental results and usage of different functionals can help us overcome the limitations of the current technology and get values closer to the ground-state energy.

The current work aims to apply a DFT-based approach in calculating the thermochemistry of the materials using a much larger number of atoms and layers for solid-phase periodic models. Popular transition metals and their oxides were chosen so that they can be used for different applications. Thermochemistry data were converted to their thermodynamic coefficients in an attempt to make them available for use in different chemical kinetic applications. The calculated data with thermodynamic properties were carefully analyzed and compared with previously calculated and experimental data.

2. METHODOLOGY

2.1. Computational Details. The thermodynamic properties of ten species were calculated using the DFT method. Most of the species were studied using crystalline models, while for La_2O_3*, an amorphous model was used to analyze and compare the behavior of species over a variety of different physical traits and innate qualities. The amorphous model is different from the crystalline model because it lacks the long-range order. Here, a nonperiodic unit cell of lanthanum oxide (La_2O_3) primitive cubic crystal (point group m3, space group la3 (206)) and lanthanum monoxide (LaO, point group $Fm\bar{3}'m$, space group 225) was taken as a reference; both of them were heated and then quenched using the amorphous cell algorithm along with a rotational isomeric state (RIS) model[23] to generate an amorphous cell of lanthanum oxide (La_2O_3*). In the amorphous cell construction calculation, a cubic-type lattice was chosen, with a density of 1.0 g/cm^3 and the output in one frame. Construction calculation was performed at 298 K with 1000 loading steps and the geometry was optimized automatically right after the cell formation at 0.1 cal/mol and 0.5 kcal/mol/Å force. A universal force field-based current was used for the amorphous cell construction and the Ewald-based summation method was used with an accuracy of 0.001 kcalmol^{-1}, while van der Waals interactions are atom-based. All DFT calculations were performed using the DMol^3 Package.[24,25] The generalized gradient approximation of Perdew−Burke−Ernzerhof (GGA-PBE)[26] and the BLYP (Becke for the exchange part, and Lee, Yang, and Parr for the correlation part)[27,28] functional were selected for exchange and correlation potentials. Due to the difference in size of the crystal and morphology, DMol^3 generates *k*-points based on equally spaced reciprocal space points depending on the length of the primitive reciprocal space lattice vectors in the first Brillouin zone. The spacing parameter is kept at the default value of 0.03 au, while the *k*-point separation was kept as 0.08 Å^{-1}; these *k*-points are specified in the form of Monkhorst−Pack grid parameters.[29] The orbital cutoffs of La, Cu, Fe, Mn, and Co are 5.0, 4.0, 4.3, 4.4, and 4.1 Å, respectively. Double numerical plus d-function (DND) and double numerical plus polarization (DNP) basis sets were used. Two different basis sets were used on the solid models, which are used for efficient conversion of partial differential functions into algebraic equations. Table S1 (see Supporting Information, SM) shows the species arrangement in ascending order of atoms. For the computation, the pressure was kept constant at 1 bar to simulate real conditions, and the practical usage dictates that 1 bar pressure should be selected to simulate maximum possible stable conditions.[30] The DMol^3 package enables us to calculate the thermodynamics through the results of the hessian evaluation, or vibrational analysis can be used to compute the enthalpy (H), entropy (S), free energy (G), and heat capacity (C_p) at a constant pressure as a function of temperature; these formulas were devised by Hirano.[31,32] The Helmholtz free energy is a function of temperature for a given structure, which can be determined through the vibrational partition function from the phonon density of states. As a result, using free energy minimization to determine the structure's temperature dependency is a logical technique. Here, the key foundation is the quasi-harmonic approximation, which assumes that the vibrational frequencies can be determined as though the atoms were vibrating purely harmonically while the cell parameters are adjusted to minimize the free energy. Previous studies have indicated that this is a reasonable approximation until a temperature of approximately half the melting point is reached. The smallest LaO unit cell comprises only two atoms, while the largest surface model, La_2O_3*(amorphous), comprises 21% LaO and 79% La_2O_3. Table S1 (see SM) shows all of the computational species arranged in an ascending arrangement of the number of atoms. These temperature-dependent thermodynamic properties can be used by converting them into NASA's seven-term polynomial coefficients. Thermodynamic properties can be converted into coefficients through the method of simultaneous regression.[21] These coefficients can be used for kinetic modeling. The crystalline surface and structures have been characterized by various researchers and play a very prominent role in different applications, including heterogenous catal-

https://doi.org/10.1021/acsomega.1c02178
ACS Omega 2021, 6, 22525−22536

ysis,[33−44] as shown in Table S2 (see SM). These peer-reviewed works were used to select the crystalline structure and its exposed surface. The thermodynamic properties of these structures are calculated through DFT. Understanding their thermodynamic behavior and surface catalytic kinetic reactions can help us better understand their role in a variety of applications.

2.2. Thermodynamic Data Generation. The thermodynamic data generated through DFT calculations will be further converted into seven-term thermodynamic coefficients using NASA-designated polynomial equations. These polynomial equations are E1−E6 (see SM). The heat capacity equations are equations E1 and E2, while the enthalpy and entropy equations are E3 and E4, and E5 and E6, respectively. These equations are used to convert the calculated thermodynamic values into NASA seven-term polynomial coefficients using the simultaneous regression developed by Zleznik and Gordon.[21] Polynomial fitting of these six equations will result in the seven-term NASA polynomial coefficients, and these polynomial coefficients are arranged in order so that they can be easily identified by chemical kinetic simulation software. Tables S3 and S4 (see SM) represent the arrangement order for a NASA seven-term polynomial format, which is also used as the input of the thermo input file for CHEMKIN package. The species calculations can be directly used for chemical kinetic calculations. The total temperature range is from 25 to 1000 K, while the mid-temperature is selected as 500 K. The temperature range from 25 to 500 K is considered as the low-temperature range and from 500 to 1000 K is considered as the high-temperature range. Coefficients a1−a5 of equations E1−E6 are calculated through polynomial fitting. These polynomial fittings were performed using PAST (free statistical software package), and a6 and a7 are calculated using a macro in excel based on simultaneous regression.[21] Table 2 reveals the data converted into the NASA seven-term polynomial format.

3. RESULTS AND DISCUSSION

The thermodynamic properties of a material represent the physical state of the system. The calculated models are based on the requirements of simulation and chemical kinetics. DFT calculation generates thermodynamic properties. These thermodynamic properties are converted into NASA-based polynomials through simultaneous regression. The properties are calculated within the range of 25−1000 K because most catalytic reactions can take place within this range. The detailed description of the calculated species and their thermodynamic properties are presented in Tables S1 and S2 (see SM). Table 1 displays the thermodynamic properties at

Table 1. Thermodynamic Properties at 298 K

material	enthalpy (H) (kcal/mol)	entropy (S) (cal/(mol·K))	heat capacity (C_p) (cal/(mol·K))	free energy (G) (kcal/mol)
LaO(unit)	2.087	5.910	7.011	0.325
CuO(111)	35.629	98.356	84.091	6.305
Cu(111)	31.531	149.560	99.032	−13.060
Mn_3O_4(unit)	58.357	175.264	133.919	6.102
La_2O_3(unit)	81.507	211.889	198.028	18.333
Fe_2O_3(pri)	80.926	222.443	199.432	14.605
Fe_3O_4(311)	84.408	220.910	191.759	18.544
Fe_3O_4(pri)	116.558	275.404	274.107	34.446
Co_3O_4(pri)	190.836	238.459	129.526	72.629
La_2O_3*	105.630	649.732	324.129	−88.088

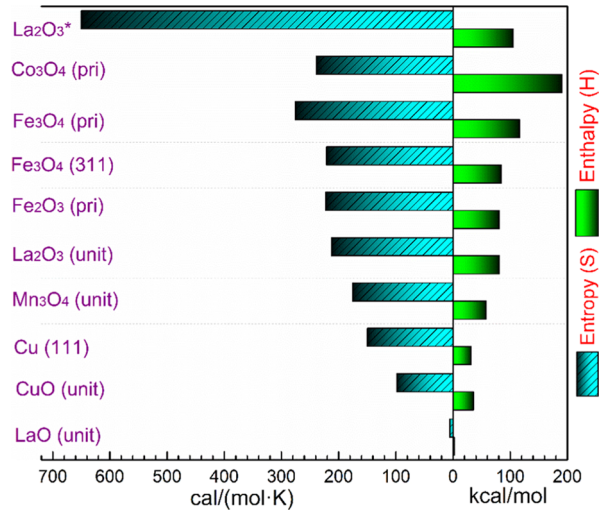

Figure 1. Entropy and enthalpy of transition metal-based species at 298 K.

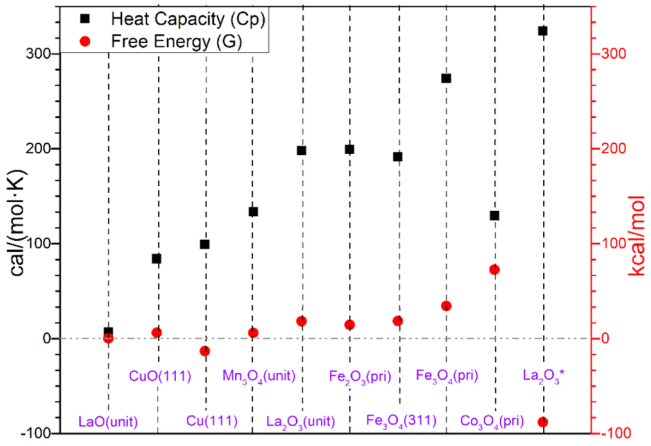

Figure 2. Heat capacity at constant pressure and free energy of the transition metal-based species at 298 K.

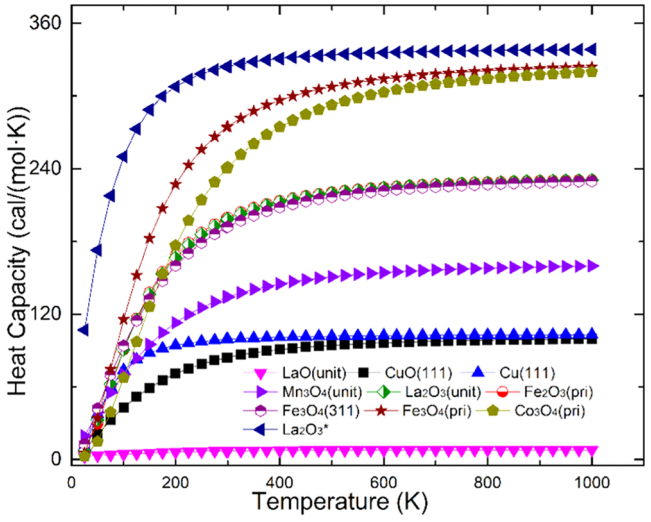

Figure 3. Heat capacity of our calculated species with temperature increment from 25 to 1000 K.

https://doi.org/10.1021/acsomega.1c02178
ACS Omega 2021, 6, 22525−22536

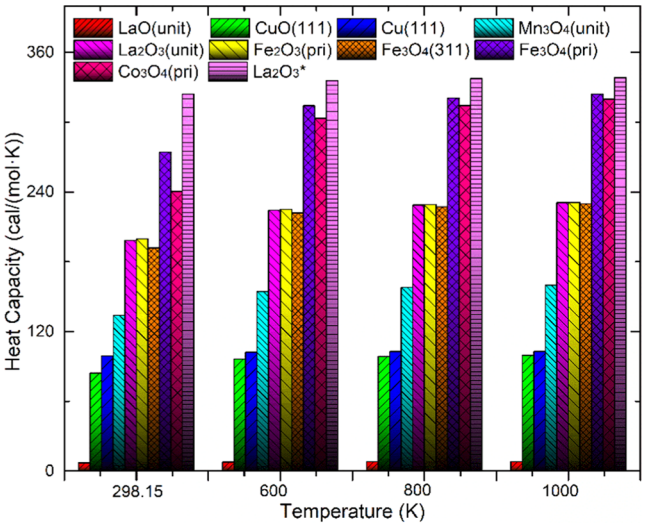

Figure 4. With C_p at a constant value, comparison of the calculated species at temperatures of 298.15, 600, 800, and 1000 K.

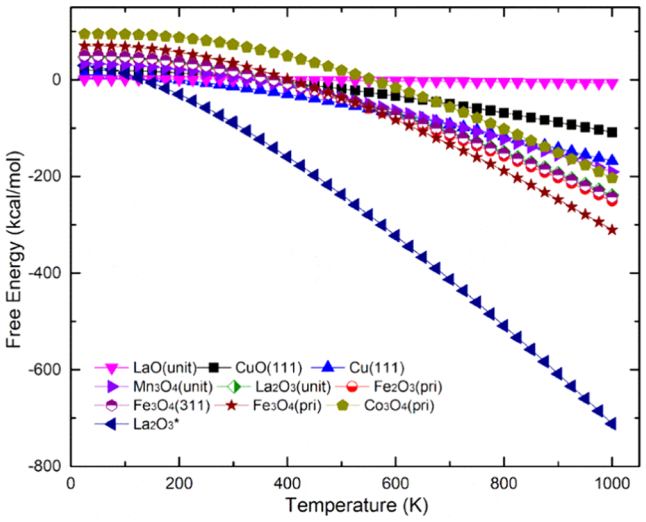

Figure 5. Free energy of the calculated species with temperature increment from 25 to 1000 K.

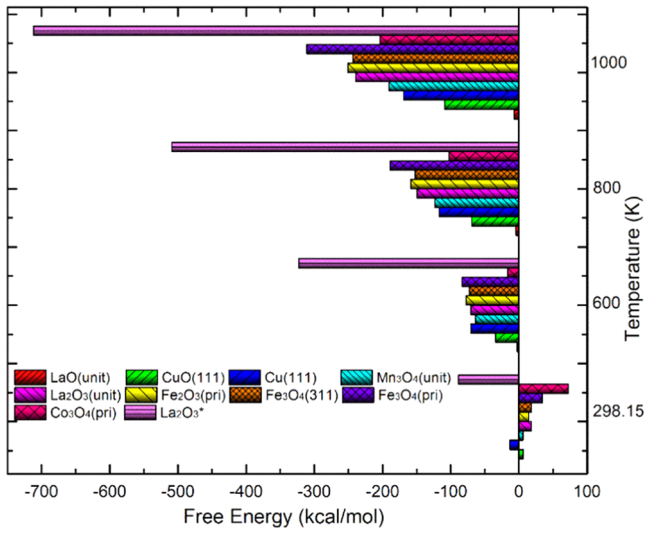

Figure 6. Free energy comparison of the calculated species at temperatures of 298.15, 600, 800, and 1000 K.

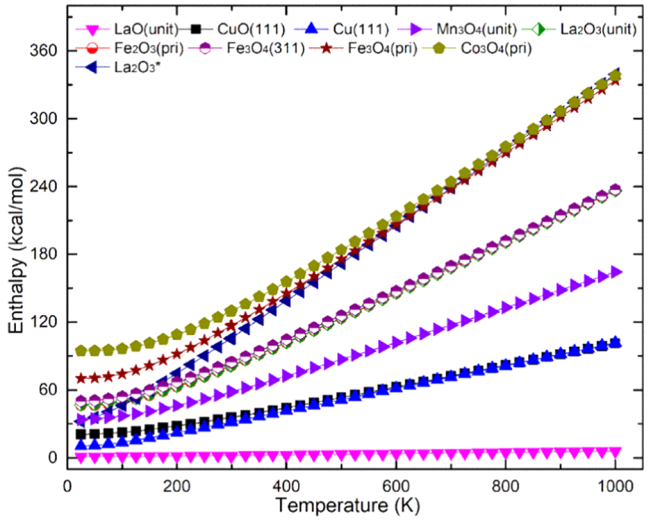

Figure 7. Enthalpy of the calculated species with temperature increment from 25 to 1000 K.

298 K (room temperature). Figures 1 and 2 show the graphical representation of H, S, C_p, and G at 298 K, respectively. H and S values tend to increase as the consecutive number of atoms is increased. The amorphous-type lanthanum-based oxide reveals the highest order of thermodynamic values as compared to its counterparts. The lowest number of atoms of a crystal presents the lowest order of values. The values of Cu(111) are higher than those of CuO(111) and LaO(111), which indicates that metal copper has higher S and C_p than its oxidized surface. Co and Fe belong to group 8 and 9 of the periodic table, respectively. The oxides of Co and Fe show dissimilar values at 298 K, which exhibit their difference of thermophysical behavior at room temperature. The values in Table 1 reveal that the thermodynamic values of a compound can be influenced by the surface lattice. Tables S5−S14 (see SM) show thermodynamic values concerning the temperature calculated through the first-principles method in detail. The thermodynamic properties of a system at 298 K represent the nature of that species at normal room conditions. These values are essential to understand their behavior for different applications. G and C_p exhibit similar trends in Table 1. In Figure 1, as the number of atoms increases from up to down in increasing order, the calculated S values at 298 K consecutively increase except for Fe_3O_4(311) and Co_3O_4(pri). However, H does not show similar trends. In Figure 2, as the structural size increases from left to right, C_p consecutively increases except for Fe_2O_3(pri) and Fe_3O_4(311). However, G does not show similar trends.

3.1. Heat Capacity (C_p). C_p calculated through DFT calculations exhibits a trend of increasing values of thermodynamics as a function of temperature. Most values stabilize at 325 K, which signifies their physical property. The heat required to raise the temperature of a specific species by 1 K is called C_p. The difference in thermophysical values reflects the behavior associated with different structures and their associated elements. The calculated C_p values of all of the transition metal-based species are reported in Figures 3 and 4. CuO(111) and Cu(111) display an increasing behavior of thermophysical properties with temperature. At 100 K, Cu(111) and CuO(111) have C_p values of 73.75 and 42.88

https://doi.org/10.1021/acsomega.1c02178
ACS Omega 2021, 6, 22525−22536

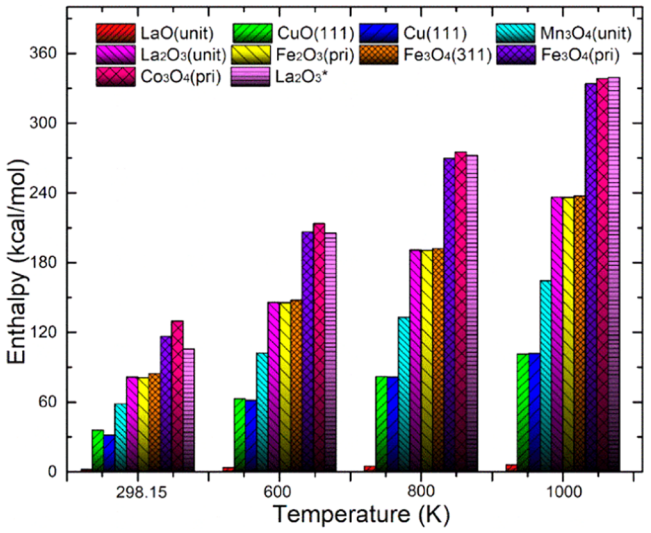

Figure 8. Enthalpy comparison of the calculated species at temperatures of 298.15, 600, 800, and 1000 K.

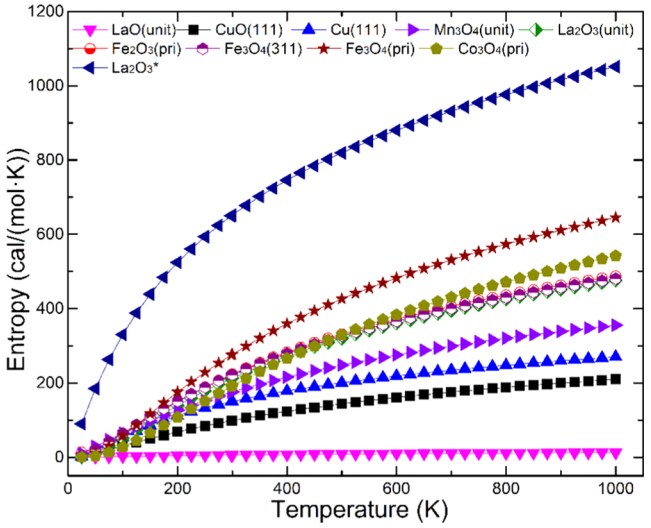

Figure 9. Entropy of the calculated species with temperature increment from 25 to 1000 K.

cal/(mol·K), respectively. At 500 K, C_p increases up to 101.76 and 94.25 cal/(mol·K), while at 1000 K, these values surge up to 102.93 and 99.45 cal/(mol·K), respectively. A temperature rise reduces the difference between the C_p values of these two species. The oxidized copper has lowered C_p values at temperatures less than 400 °C, but as the temperature increases their values become closer. Lanthanum-based species LaO(unit), La_2O_3(unit), and La_2O_3* also have different thermophysical effects. LaO(unit) exhibits a small-increment change. However, it has similar trends. La_2O_3(unit) and La_2O_3* display similar trends in terms of their heat capacity evolution as a function of temperature. At 100 K, the C_p values of La_2O_3 (unit) and La_2O_3* are 90.50 and 250.04 cal/(mol·K), respectively. At 500 K, C_p increases up to 220.05 and 333.96 cal/(mol·K), while at 1000 K, the values are 230.70 and 338.32 cal/(mol·K), respectively. Even if the structural arrangement is completely different for both species, the C_p difference becomes smaller with the increase of temperature. La_2O_3* exhibits the highest value of C_p; hence, it requires the highest amount of heat per increase in temperature. Iron-based oxides

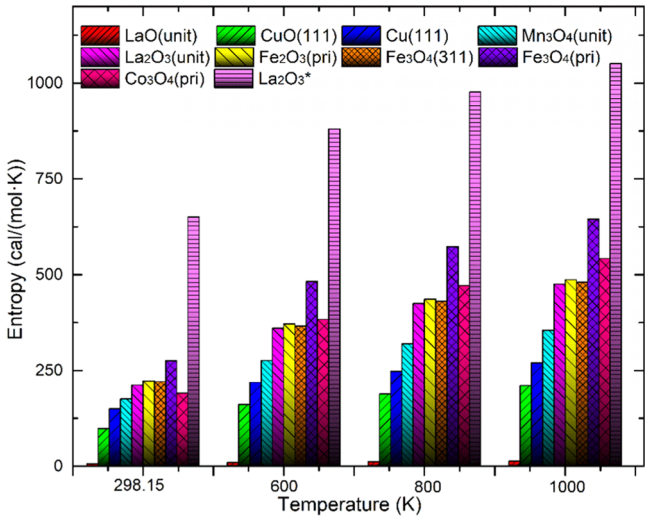

Figure 10. Entropy comparison of the calculated species at temperatures of 298.15, 600, 800, and 1000 K.

such as Fe_2O_3(pri), Fe_3O_4(311), and Fe_3O_4(pri) exhibit relative trends of C_p. Fe_3O_4(pri) and Co_3O_4(pri) reveal similar thermodynamic trends and similar C_p. La_2O_3(unit), Fe_2O_3(pri), and Fe_3O_4(311) exhibit stability in values from 325 K. Fe_3O_4(311) and Fe_3O_4(pri) present little dissimilarities in their properties due to the difference in the surface lattice.

3.2. Free Energy. The calculated G values show a decreasing trend with a consecutive increase in temperature for all species. Smaller structures display small increments of change, while larger structures express higher increments of variation in thermodynamic quantities. The order of G does not express similar trends as C_p. Concave negative curves are observed for larger structures with more atoms, while smaller structures have small variations in the values of G. The change in G value with temperature for different species displays the change in thermodynamic behavior. Figures 5 and 6 represent the Gibbs energies of the calculated species with increase in temperature. La_2O_3* exhibits the most abrupt change to negative values at 150 K, as observed in Table S12 (see SM). Co_3O_4(pri) shows change to a negative value at 575 K. Mn_3O_4(unit) and Cu(111) show a negative change in G at around 298.15 K, while others shift at higher temperatures. Figure 6 shows that most species have positive G values at 298.15 K, except for La_2O_3*, which has a negative G at 150 K. Co_3O_4(pri) has negative values at 575 K. La_2O_3* displays the most spontaneous change to negative G, while crystalline LaO(unit) is less spontaneous. These spontaneous reactions indicate the feasibility of a reaction to proceed in the forward directions. Most species shift to negative values at 550 K values, which seems to reflect the feasibility of a reaction to occur at higher temperatures. The Gibbs energy for a specific reaction or species is calculated at a specific temperature and pressure; hence, the change of temperature gives the G profile of the species. The negative G is also correlated with increasing entropy. Comparing Figures 6 and 10, It can be observed that a higher H results in lower G. LaO(unit) demonstrates almost zero-G, which indicates the stability of its structure, and no spontaneous change at all temperatures. Co_3O_4(pri) shifts to negative G at 500 K. La_2O_3* shows the quickest negative G shift. Iron-based oxides Fe_2O_3(Pri) and Fe_3O_4(311) exhibit similar values, while Fe_3O_4(pri) shows a slightly lower value of G.

https://doi.org/10.1021/acsomega.1c02178
ACS Omega 2021, 6, 22525−22536

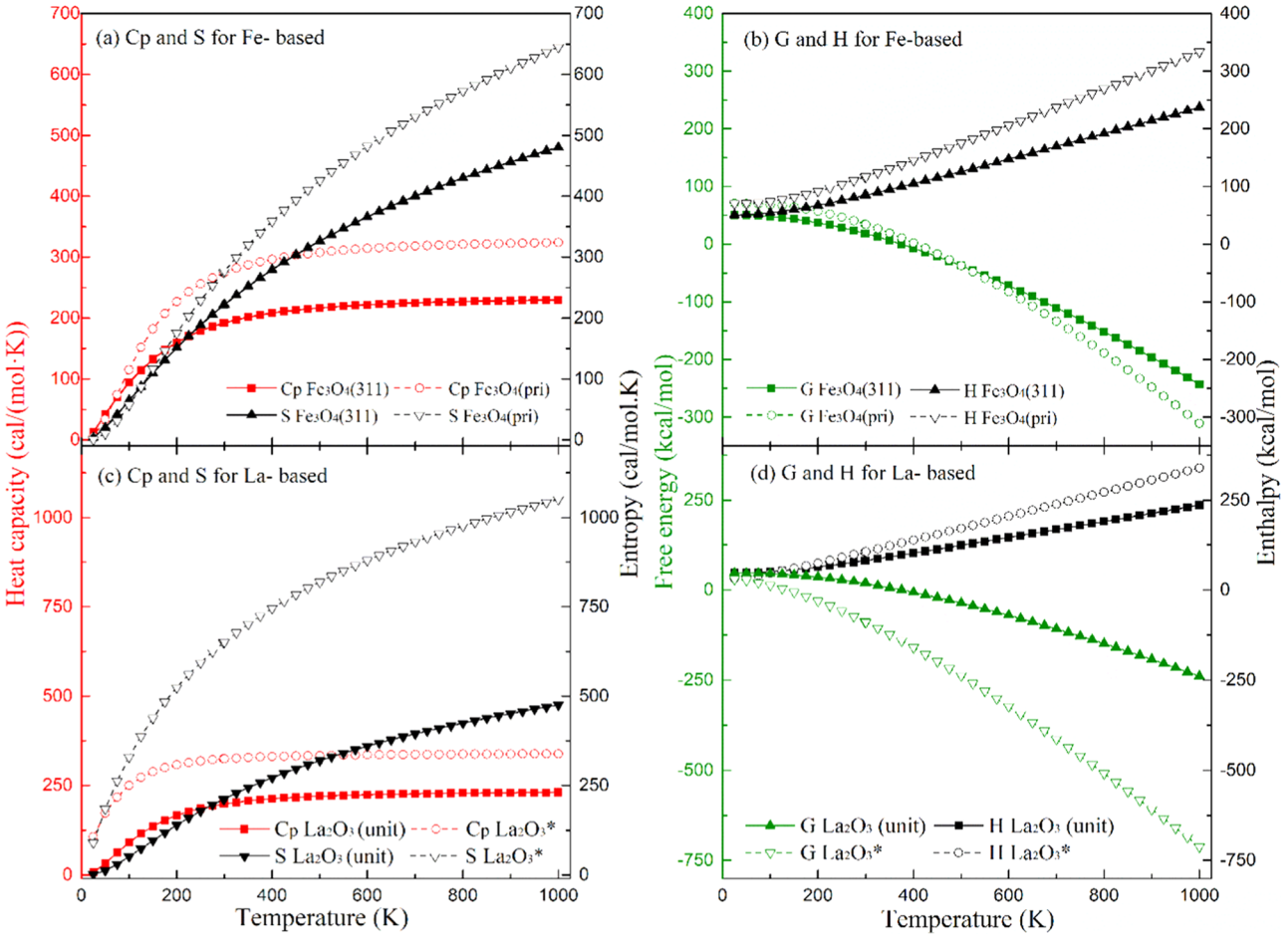

Figure 11. C_p, *S*, *H* and *G* comparison for Fe- and La-based species: (a) C_p and *S* for Fe-based oxide, (b) *G* and *H* for Fe-based oxide, (c) C_p and *S* for La-based oxide, (d) *G* and *H* for La-based oxide.

3.3. Enthalpy. The values of *H* exhibit a constant rising trend for all samples. The temperature rise of a particular system reflects its kinetic and potential energy rise, which results in increased enthalpy. As can be seen from Figure 7, LaO(unit) does not show a continuous change in *H*, while larger structures such as Co_3O_4(pri) and La_2O_3* portray a much larger change. In Figure 8, Co_3O_4(pri) shows much larger order of values at 298.15, 600, and 800 K compared with La_2O_3*, while the trend is vice versa at 1000 K. The C_p and *H* of Co_3O_4(pri) show a similar increasing trend; both show changes in peak values at 325 K, as can be seen from Figures 3 and 7. The correlation between *G* and C_p indicates that Co_3O_4 shows the highest *H* value along with a positive Gibbs energy at 500 K, while the stability of C_p is only reached at 800 K. In Figure 7, Cu(111) and its oxide CuO(111) have similar *H* values. At temperatures lower than 500 K, they reveal a small difference of *H*, whereas the oxide leads the metal by a difference of less than 5 kcal/mol. At temperatures higher than 500 K, the difference becomes less than 2 kcal/mol. For lanthanum-based species LaO(unit), La_2O_3(unit), and La_2O_3*, at 100 K, the values for La_2O_3(unit) and La_2O_3* are found to be 50.42 and 40.34 kcal/mol, while at 150 K, these values increase up to 56.06 and 59.82 kcal/mol. At 500 K, the values are 123.78 and 171.88 kcal/mol, respectively. LaO reveals similar increasing trends in small increments, while La_2O_3(unit) and La_2O_3* show a larger difference. The enthalpy of La_2O_3* exceeds that of La_2O_3(unit) at 150 K, and it steadily continues to increase. Fe and Co belong to columns 8 and 9 of the periodic table; even though they belong to different columns, their oxides show a similar behavior in properties. The enthalpies of Fe_3O_4(pri) and Co_3O_4(pri) reveal similar thermodynamic trends.

3.4. Entropy. The entropy curves display an increasing trend as a function of temperature in a concave manner, as shown in Figure 9. The increase in temperature results in a consecutive decrease in *G*, which is due to the disorder of the system, as observed in Figure 7. From Figure 5 and Table S1 (see SM), as the number of atoms increases, the enthalpy increases in a similar manner, which is similar to the entropy curves. In Figures 9 and10, LaO has the lowest values of *S*, while La_2O_3* and Fe_3O_4(pri) have the highest values. La_2O_3* is an amorphous species; the reported properties indicate that amorphous species have the highest disorder. Figures 5 and 6 display that La_2O_3* also has the highest negative *G*, which corresponds to a spontaneous change in its properties. It confirms the general behavior of amorphous materials having the highest entropy and thermodynamic properties.[45] LaO has the lowest disorder, which illustrates its stability. La_2O_3(unit) and La_2O_3* have different *S* values, which reveals that amorphous materials have more *S* and negative *G* with increasing temperature as compared to their crystalline counterparts. From the analysis of Figures 9 and 10, at 100 K, Cu(111) and CuO(111) present entropy values of 30.11 and 53.74 cal/(mol·K). At 500 K, these values become 143.75

https://doi.org/10.1021/acsomega.1c02178
ACS Omega 2021, 6, 22525−22536

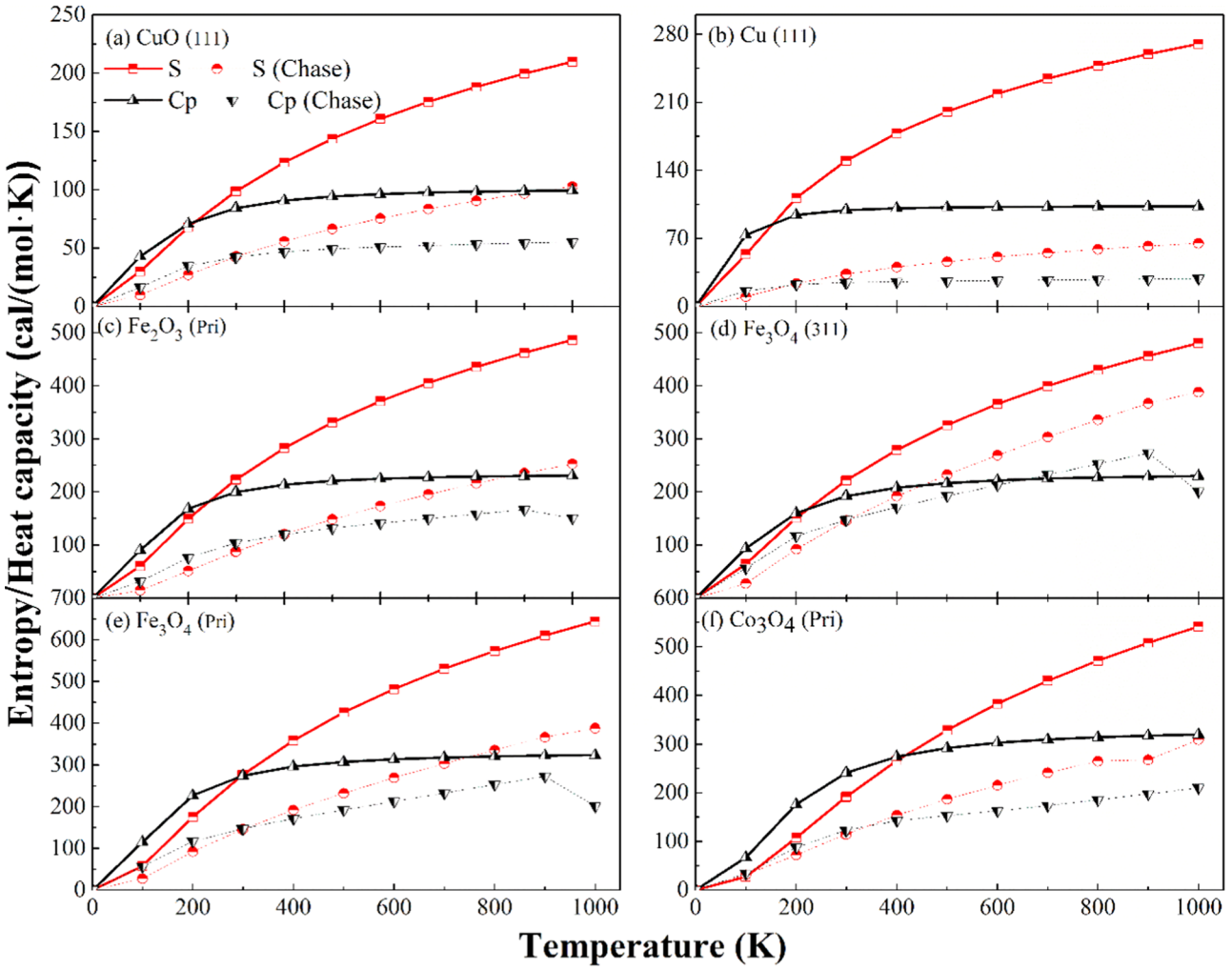

Figure 12. Comparison of the entropy (S) and heat capacity (C_p) with those from JANAF studies: (a) CuO(111); (b) Cu(111); (c) Fe_2O_3(primitive); (d) Fe_3O_4(311); (e) Fe_3O_4(primitive); and (f) Co_3O_4(primitive).

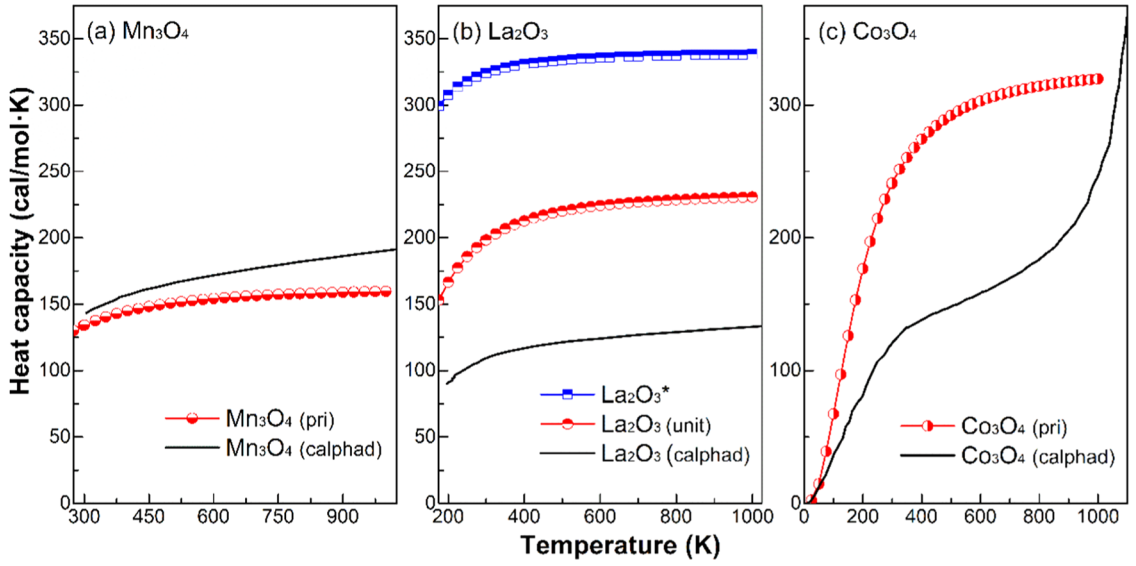

Figure 13. Comparison of the heat capacity (C_p) with thermodynamic assessments by CALPHAD with those from other studies: (a) Mn_3O_4(pri); (b) La_2O_3(unit)/La_2O_3*; and (c) Co_3O_4(pri).

and 200.55 cal/(mol·K), while at 1000 K, they are 209.87 and 270.21 cal/(mol·K), respectively. It can be noted that Cu(111) and CuO(111) exhibit similar trends in S values, while values for their oxide species exceed those of the metal at all

https://doi.org/10.1021/acsomega.1c02178
ACS Omega 2021, 6, 22525−22536

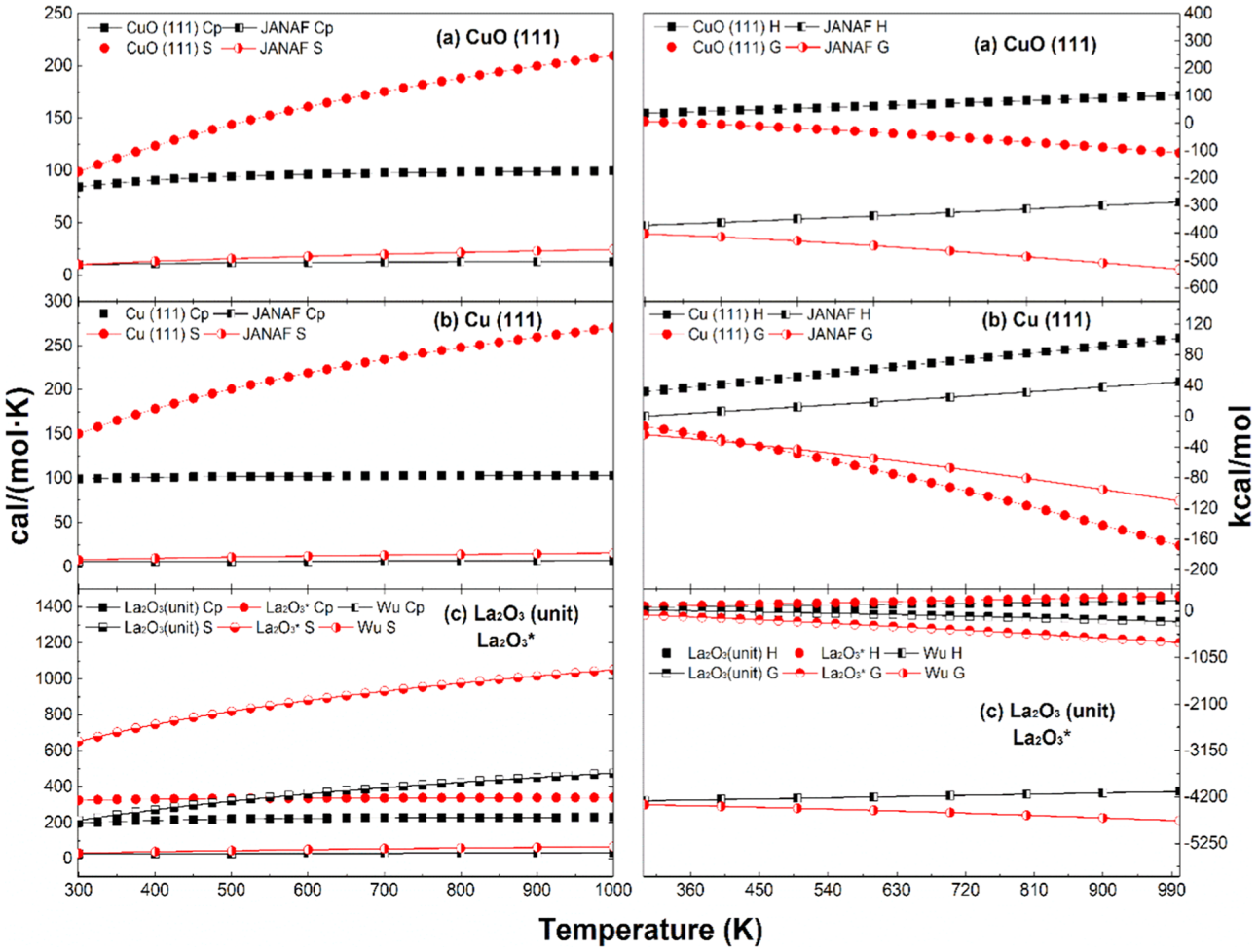

Figure 14. Comparison of the thermodynamic values with those of different studies: (a) CuO(111); (b) Cu; and (c) La_2O_3 (unit) and La_2O_3*.

temperatures. For lanthanum-based species, La_2O_3(unit) and La_2O_3* show different entropies, which reflects the disorders of the materials due to their structural differences. Comparing the values of cobalt and iron for Co_3O_4(pri) and Fe_3O_4(pri) from Figures 3, 7, and 9, the performance of entropy is different when compared with H and C_p. It reflects the disorder of the species' inert property. Fe_2O_3(pri) and Fe_3O_4(311) report similar trends and values of S at all temperatures.

3.5. Comparison Based on the Surface Lattice and Types of Solids. The correlation among thermodynamic properties, morphological order, and lattice parameters is shown in Figure 11. Fe_3O_4(pri) is a primitive cell, while Fe_3O_4(311) is a surface lattice site. La_2O_3(unit) is crystalline, while La_2O_3* is amorphous. The C_p, S, and H for Fe_3O_4(pri) are higher as compared to those for Fe_3O_4(311). The G of Fe_3O_4(pri) is higher than that of Fe_3O_4(311) at 1000 K, and vice versa for values less than 500 K. Both the surface lattice and unit cell show changes in properties as a function of temperature. La_2O_3* has higher thermodynamic values as compared to La_2O_3(unit), which reveals that it has a higher C_p, H, and S but much lower G. These high-end thermodynamic properties indicate the general behavior of an amorphous material, which is well observed here by comparing them with their crystalline counterparts.[45]

4. COMPARISON WITH OTHER STUDIES

Upon careful comparison with the thermodynamic properties calculated by Chase[30] and thermodynamic assessment calculated through CALPHAD codes,[46−48] as displayed in Figures 12 and 13, it can be observed that the C_p and S values reveal similar trends to the ones reported in the literature.[30] The solid-phase periodic model calculations have comparatively higher thermodynamic values of C_p and S, when compared with the gas-phase models in JANAF.[30] CALPHAD models are designed to use computational algorithms for the development of phase diagrams. They use experimental results from various resources to effectively calculate accurate phase diagrams.[49,50] In Figure 13a, Mn_3O_4(pri) is compared with Mn_3O_4(calphad), which shows that the code-generated values are closer to the ones calculated in the current work. For temperatures below ∼600 °C, it can be observed that Mn_3O_4(pri) calculated values have an error of less than 5%, while the values tend to show a higher discrepancy at higher temperatures. In Figure 13b, La_2O_3(unit) and La_2O_3* are compared with the values generated through CALPHAD codes. La_2O_3(calphad) shows a lower order of values as compared to those from the literature. These values can be brought closer by calculating the thermodynamic data of individual species through differential functional groups. In Figure 13c, it can be observed that Co_3O_4(pri) has similar values at temperatures less than ∼200 °C and higher than ∼900 °C, while there is greater discrepancy in-between these

https://doi.org/10.1021/acsomega.1c02178
ACS Omega 2021, 6, 22525−22536

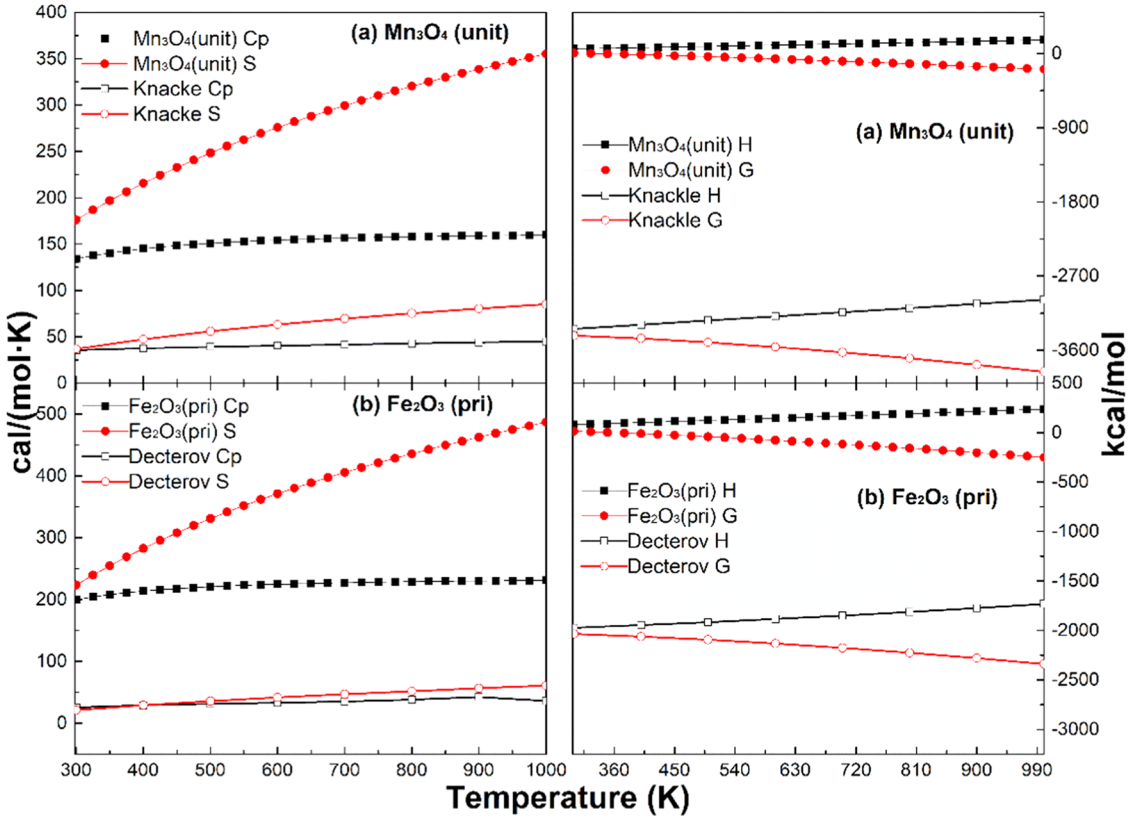

Figure 15. Comparison of the thermodynamic values with those of different studies: (a) Mn_3O_4(unit) and (b) Fe_2O_3(pri).

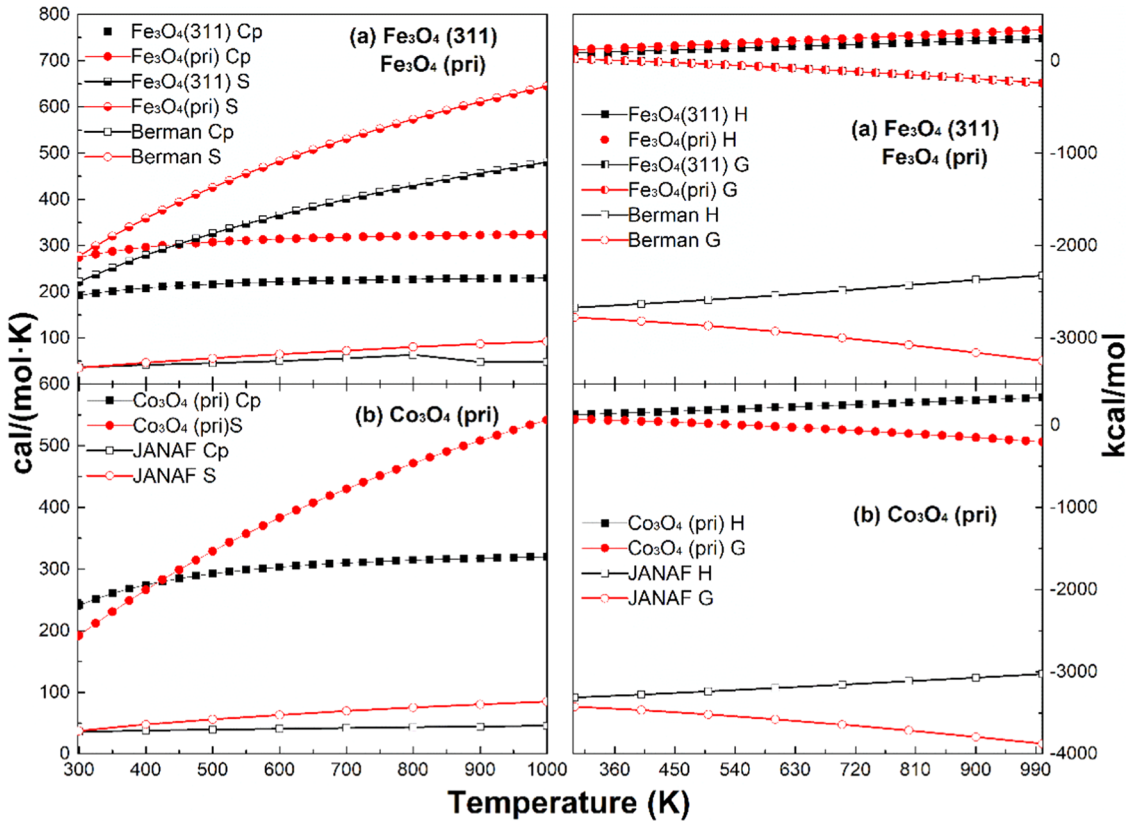

Figure 16. Comparison of the thermodynamic values with those of different studies: (a) Fe_3O_4(311) and Fe_3O_4(pri); (b) Co_3O_4(pri).

temperatures. These errors could be removed through calculations of these species using different functional groups.

Furthermore, a comparison of the calculated results with the data from literature has been performed. Figure 14 compares

https://doi.org/10.1021/acsomega.1c02178
ACS Omega 2021, 6, 22525−22536

Table 2. Generated NASA Seven-term Polynomial Format Calculated through Ab Initio Calculations

CuO(111)	CuO	O	1Cu	1	0	0S	25.00	1000.00	500.00	1
	2.71163200×10	$8.49600000 \times 10^{-2}$	$-1.27650000 \times 10^{-4}$	$9\ 04814000 \times 10^{-8}$	$-2.48585000 \times 10^{-11}$					2
	$-4.46439977 \times 10^{4}$	$-1.26768178 \times 10^{2}$	-4.20852000	$3.37210000 \times 10^{-1}$	$-8.95395000 \times 10^{-4}$					3
	$1.13032000 \times 10^{-6}$	$-5.50026000 \times 10^{-10}$	1.47937122×10	6.37684253						4
LaO (unit)	LaO	O	1La	1	0	0S	25.00	1000.00	500.00	1
	2.68580000	$4.79000000 \times 10^{-3}$	$-7.33684000 \times 10^{-6}$	$5.27775000 \times 10^{-9}$	$-1.46728000 \times 10^{-12}$					2
	$-3.65811935 \times 10^{3}$	-1.46919220×10	$7.81530000 \times 10^{-1}$	$1.71100000 \times 10^{-2}$	$-2.92337000 \times 10^{-12}$					3
	$2.50364000 \times 10^{-9}$	$2.37964000 \times 10^{-11}$	-2.41372839×10	-2.89250634						4
Cu(111)	Cu	O	1Cu	1	0	0S	25.000	1000.00	500.000	1
	4.60861000×10	$2.19200000 \times 10^{-2}$	$-3.38482000 \times 10^{-5}$	$2.44625000 \times 10^{-8}$	$-6.81928000 \times 10^{-12}$					2
	$-5.04639313 \times 10^{4}$	$-1.93806309 \times 10^{2}$	-1.13161000×10	$7.70030000 \times 10^{-1}$	$-3.65000000 \times 10^{-3}$					3
	$7.54915000 \times 10^{-6}$	$-5.68936000 \times 10^{-9}$	6.57733681×10	1.94322469×10						4
Mn3O4 (pri)	Mn_3O_4	O	1Mn	1	0	0S	25.000	1000.00	500.000	1
	8.34087300×10	$2.79970000 \times 10^{-1}$	$-4.17595000 \times 10^{-4}$	$2.94420000 \times 10^{-7}$	$-8.05562000 \times 10^{-11}$					2
	$-1.41606458 \times 10^{5}$	$-5.46607782 \times 10^{2}$	-2.55035000	$9.29650000 \times 10^{-1}$	$-2.20000000 \times 10^{-3}$					3
	$2.34505000 \times 10^{-6}$	$-8.54200000 \times 10^{-10}$	$-1.98519843 \times 10^{2}$	-8.97262445						4
La_2O_3(unit)	La_2O_3	O	1La	1	0	0S	25.000	1000.00	500.000	1
	1.34171370×10^{2}	$3.61580000 \times 10^{-1}$	$-5.48023000 \times 10^{-4}$	$3.90769000 \times 10^{-7}$	$-1.07807000 \times 10^{-10}$					2
	$-2.08298948 \times 10^{5}$	$-8.78483692 \times 10^{2}$	-5.88202900×10	2.06399000	$-6.34000000 \times 10^{-3}$					3
	$9.33664000 \times 10^{-6}$	$-5.36738000 \times 10^{-9}$	8.81279130×10^{2}	1.40210125×10^{2}						4
Fe_2O_3(pri)	Fe_2O_3	O	1Fe	1	0	0S	25.000	1000.00	500.000	1
	6.95143600×10	$1.75260000 \times 10^{-1}$	$-2.66071000 \times 10^{-4}$	$1.89925000 \times 10^{-7}$	$-5.24360000 \times 10^{-11}$					2
	$-1.05329238 \times 10^{5}$	$-3.27686001 \times 10^{2}$	-1.71754800×10	$7.68630000 \times 10^{-1}$	$-1.39000000 \times 10^{-3}$					3
	$8.29094000 \times 10^{-8}$	$1.29839000 \times 10^{-9}$	2.19693862×10^{2}	4.28022436×10						4
Fe_3O_4(311)	Fe_3O_4	O	1Fe	1	0	0S	25.000	1000.00	500.000	1
	5.90216600×10	$2.08510000 \times 10^{-1}$	$-3.11881000 \times 10^{-4}$	$2.20316000 \times 10^{-7}$	$-6.03635000 \times 10^{-11}$					2
	$-1.02203167 \times 10^{5}$	$-2.76811189 \times 10^{2}$	-1.18633900×10	$7.62510000 \times 10^{-1}$	$-1.91000000 \times 10^{-3}$					3
	$2.20329000 \times 10^{-6}$	$-9.22281000 \times 10^{-10}$	9.33464529×10	2.15444459×10						4
Fe_3O_4(pri)	Fe_3O_4	O	1Fe	1	0	0S	25.000	1000.00	500.000	1
	8.88471000×10	$2.77310000 \times 10^{-1}$	$-4.19455000 \times 10^{-4}$	$2.98687000 \times 10^{-7}$	$-8.23266000 \times 10^{-11}$					2
	$-1.45722196 \times 10^{5}$	$-4.35883015 \times 10^{2}$	-2.49267100×10	$9.82720000 \times 10^{-1}$	$-1.34000000 \times 10^{-3}$					3
	$-1.22506000 \times 10^{-6}$	$2.83521000 \times 10^{-9}$	3.58464990×10^{2}	5.64159380×10						4
Co_3O_4(pri)	Co_3O_4	O	Co	1	0	0S	25.000	1000.00	500.000	1
	8.88471000×10	$2.77310000 \times 10^{-1}$	$-4.19455000 \times 10^{-4}$	$2.98687000 \times 10^{-7}$	$-8.23266000 \times 10^{-11}$					2
	$-1.45720018 \times 10^{5}$	$-4.87618798 \times 10^{2}$	-2.49267100×10	$9.82720000 \times 10^{-1}$	$-1.34000000 \times 10^{-3}$					3
	$-1.22506000 \times 10^{-6}$	$2.83521000 \times 10^{-9}$	3.70781044×10^{2}	5.61235374×10						4
La_2O_3*	La_2O_3	O	1La	1	0	0S	25.000	1000.00	500.000	1
	2.96764660×10^{2}	$1.58440000 \times 10^{-1}$	$-2.43599000 \times 10^{-4}$	$1.75509000 \times 10^{-7}$	$-4.88041000 \times 10^{-11}$					2
	$-3.28730654 \times 10^{5}$	$-1.60389747 \times 10^{3}$	3.69975400×10	3.31829000	$-1.48200000 \times 10^{-2}$					3
	$2.96812000 \times 10^{-5}$	$-2.19225000 \times 10^{-8}$	$-1.87139521 \times 10^{3}$	-8.97262445						4

the thermodynamic properties of CuO(111), Cu(111), and La_2O_3(unit)/La_2O_3* with the data reported by JANAF[51] and Wu.[52] The calculated values exhibit similar trends to the literature ones. C_p and S show a difference of ±100 cal/(mol·K), while H and G show a difference of ±200 kcal/mol, as shown in Figure 14a. The calculated C_p and S values and reported data indicate a difference of ±100 cal/(mol·K), while H and G show a difference of ±50 kcal/mol (Figure 14b). The calculated data show a difference of ±200 cal/(mol·K) for La_2O_3 and ±600 cal/(mol·K) for La_2O_3* for C_p and S, respectively, whereas H and G show slightly larger differences. Comparison with experimental data has been done through analysis of the work done by Knacke,[53] Decterov,[54] and Berman.[55] Figure 15 compares the thermodynamic properties of Mn_3O_4(unit) and Fe_2O_3(pri) with those from Knacke[53] and Decterov.[54] Mn_3O_4(111) shows a difference of ±150 cal/(mol·K) for C_p and S, but larger differences for H and G. Fe_2O_3(pri) tends to show ±200 cal/(mol·K) difference for both C_p and S, while there is a difference of ±2000 kcal/mol for both H and G. Figure 16 compares the thermodynamic properties of Fe_3O_4(311)/Fe_3O_4(pri) and Co_3O_4(pri) with the values from Berman[55] and JANAF.[51] In Figure 16a,b, Fe_3O_4(unit), Fe_2O_3(unit), and Co_3O_4 show similar trends to JANAF. The calculated values show a difference of about ±200 cal/(mol·K) for C_p and S, while H and G have differences of ±3000 kcal/mol. The comparison shows similar trends for the calculated thermodynamic properties but the values differ positively or negatively. These changes in properties are due to the current limitations of computational resources. These variations can greatly affect the calculations. Further calculations using different functional groups can help to find the model and properties closer to experimental data.

5. NASA SEVEN-TERM POLYNOMIAL FORMAT

The thermodynamic values generated through DFT calculations are converted into a NASA seven-term polynomial format through simultaneous regression by using equations E1−E6 (see SM). These values were calculated using a similar strategy as in the literature.[11,12] Table 2 represents the thermodynamic coefficients calculated through ab initio

https://doi.org/10.1021/acsomega.1c02178
ACS Omega 2021, 6, 22525−22536

calculations. These thermodynamic coefficients can be used for understanding the chemical kinetics in heterogeneous models and can give insights into the simulation and experimental behavior of popular material species.

6. CONCLUSIONS

Thermochemistry calculations were performed based on ground-state energy calculations and thermal corrections at different temperatures. Analysis of these thermodynamic properties points out the behavior of these materials based on their S, H, C_p, and G. A higher number of atoms tends to own larger thermodynamic values. The S and H of most species express similar trends with increasing temperature. Amorphous La_2O_3* exhibits higher thermodynamic values as compared to its crystalline form. LaO(unit) and Co_3O_4(pri) have positive G at higher temperatures, while La_2O_3* and Cu(111) have negative G at 298 K. The negative G at low temperatures represents the abrupt reactive behavior of these materials. Thermodynamic values vary based on different lattice parameters and arrangement of atoms. The calculated values present similar trends to the values reported in the literature. The calculated thermodynamic parameters and thermodynamic coefficients for transition metal-based species offer the opportunity for a better understanding of metal oxides and their thermodynamics. These surface thermodynamic coefficients can be used for different thermodynamic calculations. The quality of the thermodynamic values can be improved by calculating over larger surfaces and using the appropriate correlation functions. Moreover, the strategy developed in the present work could be further applied to obtain the surface thermochemistry of other materials.

■ ASSOCIATED CONTENT

Supporting Information

The Supporting Information is available free of charge at https://pubs.acs.org/doi/10.1021/acsomega.1c02178.

Details of the used equations from E1 to E6; parameter tables for surface species along with its calculation and arrangement of generated polynomial coefficient from Tables S1 to S4; tables of the generated thermodynamic data for all calculated species from Tables S5 to S13 (PDF)

■ AUTHOR INFORMATION

Corresponding Author

Zhen-Yu Tian − *Institute of Engineering Thermophysics, Chinese Academy of Sciences, Beijing 100190, China; University of Chinese Academy of Sciences, Beijing 100049, China;* orcid.org/0000-0003-1497-3762; Phone: +86-10-82543305; Email: tianzhenyu@iet.cn

Authors

Muhammad Fahad Arshad − *Institute of Engineering Thermophysics, Chinese Academy of Sciences, Beijing 100190, China; University of Chinese Academy of Sciences, Beijing 100049, China*

Ling-Nan Wu − *Institute of Engineering Thermophysics, Chinese Academy of Sciences, Beijing 100190, China*

Achraf El Kasmi − *Institute of Engineering Thermophysics, Chinese Academy of Sciences, Beijing 100190, China; Laboratory LSIA, UAE/U02ENSAH, National School of Applied Sciences of Al Hoceima, Abdelmalek Essaadi University, Al Hoceima 32003, Morocco;* orcid.org/0000-0002-0037-2328

Wu Qin − *National Laboratory for Biomass Power Generation Equipment, North China Electric Power University, Beijing 102206, China*

Complete contact information is available at: https://pubs.acs.org/10.1021/acsomega.1c02178

Notes

The authors declare no competing financial interest.

■ ACKNOWLEDGMENTS

The authors thank the financial support from the Ministry of Science and Technology of China (2017YFA0402800), Natural Science Foundation of China (No. 51976216/51888103), Beijing Municipal Natural Science Foundation (JQ20017), and K.C. Wong Education Foundation and Recruitment Program of Global Youth Experts. Muhammad Fahad Arshad thanks the CAS-TWAS Scholarship program and the support of the Chinese Academy of Sciences. Achraf El Kasmi thanks the support of the Chinese Academy of Sciences for senior international scientists (Grant No. 2017PE009) and the CAS project (Grant No. 2018/43). The authors are also thankful to Prof. Yufei Zhao from the Beijing University of Chemical Technology for his support in the DFT calculations.

■ REFERENCES

(1) Zeck, S.; Wolf, D. Requirements of Thermodynamic Data in the Chemical Industry. *Fluid Phase Equilib.* **1993**, *82*, 27−38.

(2) Skiborowski, M.; Temmann, P.; Brandenbusch, C. Analyzing the Link between GE-Model Parameter Regression and Optimal Process Design. In *Comput.-Aided Chem. Eng.*; Friedl, A.; Klemeš, J. J.; Radl, S.; Varbanov, P. S.; Wallek, T., Eds.; European Symposium on Computer Aided Process Engineering; Elsevier, 2018; Vol. *43*, pp 103−108.

(3) Mallard, E.; Le Chatelier, H. L. Thermal Model for Flame Propagation. *Ann. Mines.* **1883**, *4*, 379−568.

(4) Lewis, G. N.; Randall, M. *Thermodynamics and the Free Energy of Chemical Substances*; McGraw-Hill, 1923.

(5) West, C. J.; Hull, C. *International Critical Tables of Numerical Data, Physics, Chemistry and Technology*, 1933.

(6) Rossini, F. D. *Selected Values of Properties of Hydrocarbons*; U. S. Department of Commerce, National Bureau of Standards, 1947.

(7) Perini, L. L. *Curve Fits of JANAF Thermochemical Data*; Johns Hopkins Univ., Silver SpringMd. (USA). Applied Physics Laboratory, 1972.

(8) McBride, B.; Gordon, S. *NASA Technical Note D-4097*; Cleveland, OH, August, 1967.

(9) Gardiner, W. C.; Burcat, A. *Combustion Chemistry*; Springer, 1984.

(10) McBride, B. J. *Coefficients for Calculating Thermodynamic and Transport Properties of Individual Species*; NASA Langley Research Center, 1993; Vol. *4513*.

(11) Burcat, A.; Ruscic, B. *Third Millenium Ideal Gas and Condensed Phase Thermochemical Database for Combustion (with Update from Active Thermochemical Tables)*; Argonne National Lab.(ANL): Argonne, IL (United States), 2005.

(12) Goos, E.; Burcat, A.; Ruscic, B. *Extended Third Millennium Ideal Gas and Condensed Phase Thermochemical Database for Combustion with Updates from Active Thermochemical Tables*; German Aerospace Center, Institute of Combustion Technology: Stuttgart, Germany, accessed Aug 2010, 2018; Vol. *2*.

(13) Kung, H. H. *Transition Metal Oxides: Surface Chemistry and Catalysis*, 1st ed.; Elsevier, 1989; Vol. *45*.

(14) Pienta, N. J. *Chemistry: Molecules, Matter, and Change, (Jones, Loretta; Atkins, Peter)*; ACS Publications, 2001.

(15) Ochterski, J. W. *Thermochemistry in Gaussian*; Gaussian Inc: 2000; Vol. *1*, pp 1−19.
(16) Gossett, E.; Toher, C.; Oses, C.; Isayev, O.; Legrain, F.; Rose, F.; Zurek, E.; Carrete, J.; Mingo, N.; Tropsha, A.; Curtarolo, S. AFLOW-ML: A RESTful API for Machine-Learning Predictions of Materials Properties. *Comput. Mater. Sci.* **2018**, *152*, 134−145.
(17) Nath, P.; Usanmaz, D.; Hicks, D.; Oses, C.; Fornari, M.; Buongiorno Nardelli, M.; Toher, C.; Curtarolo, S. AFLOW-QHA3P: Robust and Automated Method to Compute Thermodynamic Properties of Solids. *Phys. Rev. Mater.* **2019**, *3*, No. 073801.
(18) Aieta, C.; Gabas, F.; Ceotto, M. An Efficient Computational Approach for the Calculation of the Vibrational Density of States. *J. Phys. Chem. A* **2016**, *120*, 4853−4862.
(19) Červinka, C.; Fulem, M.; Stoffel, R. P.; Dronskowski, R. Thermodynamic Properties of Molecular Crystals Calculated within the Quasi-Harmonic Approximation. *J. Phys. Chem. A* **2016**, *120*, 2022−2034.
(20) Deutschmann, O. *Modeling and Simulation of Heterogeneous Catalytic Reactions: From the Molecular Process to the Technical System*; John Wiley & Sons, 2013.
(21) Zeleznik, F. J.; Gordon, S. *Simulations Least-Squares Approximation of a Function and Its First Integrals with Application to Thermodynamic Data*; National Aeronautics and Space Administration, 1961.
(22) McBride, B. J.. *FORTRAN IV Program for Calculation of Thermodynamic Data*; National Aeronautics and Space Administration: https://ntrs.nasa.gov/api/citations/19670025863/downloads/19670025863.pdf, 1967.
(23) Flory, P. J.; Volkenstein, M. Statistical Mechanics of Chain Molecules. *Biopolymers* **1969**, *8*, 699−700.
(24) Delley, B. An All-electron Numerical Method for Solving the Local Density Functional for Polyatomic Molecules. *J. Chem. Phys.* **1990**, *92*, 508−517.
(25) Delley, B. From Molecules to Solids with the DMol3 Approach. *J. Chem. Phys.* **2000**, *113*, 7756−7764.
(26) Perdew, J. P.; Burke, K.; Ernzerhof, M. Generalized Gradient Approximation Made Simple. *Phys. Rev. Lett.* **1996**, *77*, 3865−3868.
(27) Becke, A. D. Density-Functional Exchange-Energy Approximation with Correct Asymptotic Behavior. *Phys. Rev. A* **1988**, *38*, 3098.
(28) Lee, C.; Yang, W.; Parr, R. G. Development of the Colle-Salvetti Correlation-Energy Formula into a Functional of the Electron Density. *Phys. Rev. B* **1988**, *37*, 785.
(29) Monkhorst, H. J.; Pack, J. D. Special Points for Brillouin-Zone Integrations. *Phys. Rev. B* **1976**, *13*, 5188.
(30) Chase, M. W., Jr NIST-JANAF Thermochemical Tables. *J. Phys. Chem. Ref. Data* **1998**.
(31) Hirano, T. *MOPAC Manual*; 1993.
(32) Stewart, J. J. *MOPAC 93.00 Manual*; Fujitsu Limited: Tokyo, Japan, 1993; pp 152−154.
(33) Álvarez-Galván, M. C.; de la Peña O'Shea, V. A.; Arzamendi, G.; Pawelec, B.; Gandía, L. M.; Fierro, J. L. G. Methyl Ethyl Ketone Combustion over La-Transition Metal (Cr, Co, Ni, Mn) Perovskites. *Appl. Catal., B* **2009**, *92*, 445−453.
(34) Matsui, N.; Anzai, K.; Akamatsu, N.; Nakagawa, K.; Ikenaga, N.; Suzuki, T. Reaction Mechanisms of Carbon Dioxide Reforming of Methane with Ru-Loaded Lanthanum Oxide Catalyst. *Appl. Catal., A.* **1999**, *179*, 247−256.
(35) Pisecny, P.; Husekova, K.; Frohlich, K.; Harmatha, L.; Soltys, J.; Machajdik, D.; Espinos, J. P.; Jergel, M.; Jakabovic, J. Growth of Lanthanum Oxide Films for Application as a Gate Dielectric in CMOS Technology. *Mater. Sci. Semicond. Process.* **2004**, *7*, 231−236.
(36) El Kasmi, A.; Pan, G. F.; Wu, L. N.; Tian, Z. Y. An Efficient and Innovative Catalytic Reactor for VOCs Emission Control. *Sci. Bull.* **2019**, *64*, 625−633.
(37) Grundner, S.; Luo, W.; Sanchez-Sanchez, M.; Lercher, J. A. Synthesis of Single-Site Copper Catalysts for Methane Partial Oxidation. *Chem. Commun.* **2016**, *52*, 2553−2556.
(38) Ren, J.; Hao, P.; Sun, W.; Shi, R.; Liu, S. Ordered Mesoporous Silica-Carbon-Supported Copper Catalyst as an Efficient and Stable Catalyst for Catalytic Oxidative Carbonylation. *Chem. Eng. J.* **2017**, *328*, 673−682.
(39) Tian, Z. Y.; Mountapmbeme Kouotou, P.; Bahlawane, N.; Tchoua Ngamou, P. H. Synthesis of the Catalytically Active Mn3O4 Spinel and Its Thermal Properties. *J. Phys. Chem. C* **2013**, *117*, 6218−6224.
(40) Sollier, B. M.; Gómez, L. E.; Boix, A. V.; Miró, E. E. Oxidative Coupling of Methane on Cordierite Monoliths Coated with Sr/La_2O_3 Catalysts. Influence of Honeycomb Structure and Catalyst-Cordierite Chemical Interactions on the Catalytic Behavior. *Appl. Catal., A* **2018**, *550*, 113−121.
(41) Li, K.; Chang, X.; Pei, C.; Li, X.; Chen, S.; Zhang, X.; Assabumrungrat, S.; Zhao, Z. J.; Zeng, L.; Gong, J. Ordered Mesoporous Ni/La_2O_3 Catalysts with Interfacial Synergism towards CO_2 Activation in Dry Reforming of Methane. *Appl. Catal., B.* **2019**, *259*, No. 118092.
(42) Kouotou, P. M.; Tian, Z. Y. Controlled Synthesis of α-Fe2O3@ Fe3O4 Composite Catalysts for Exhaust Gas Purification. *Proc. Combust. Inst.* **2019**, *37*, 5445−5453.
(43) Kouotou, P. M.; Vieker, H.; Tian, Z. Y.; Ngamou, P. H. T.; Kasmi, A. E.; Beyer, A.; Gölzhäuser, A.; Kohse-Höinghaus, K. Structure−Activity Relation of Spinel-Type Co−Fe Oxides for Low-Temperature CO Oxidation. *Catal. Sci. Technol.* **2014**, *4*, 3359−3367.
(44) Arshad, M. F.; El Kasmi, A.; Waqas, M.; Tian, Z. Y. Insight into One-Step Synthesis of Active Amorphous La-Co Thin Films for Catalytic Oxidation of CO. *App. Energy Combust. Sci.* **2021**, *5*, No. 100021.
(45) Graeser, K. A.; Patterson, J. E.; Zeitler, J. A.; Rades, T. The Role of Configurational Entropy in Amorphous Systems. *Pharmaceutics* **2010**, *2*, 224−244.
(46) Chen, M.; Hallstedt, B.; Gauckler, L. J. Thermodynamic Assessment of the Co-O System. *JPE* **2003**, *24*, 212−227.
(47) Grundy, A. N.; Hallstedt, B.; Gauckler, L. J. Thermodynamic Assessment of the Lanthanum-Oxygen System. *JPE* **2001**, *22*, 105−113.
(48) Wang, M.; Sundman, B. Thermodynamic Assessment of the Mn-O System. *Metall. Trans. B* **1992**, *23*, 821−831.
(49) Lukas, H. L.; Fries, S. G.; Sundman, B. *Computational Thermodynamics: The CALPHAD Method*; Cambridge University Press: Cambridge, 2007.
(50) Liu, Z.-K. First-Principles Calculations and CALPHAD Modeling of Thermodynamics. *J. Phase Equilibria Diffus* **2009**, *30*, 517.
(51) Tables, J. T. By DR Stull and H. Prophet (US Department of Commerce, Washington, 1985). Cp Fitted by CRCT, Montreal, 1971.
(52) Wu, P.; Pelton, A. D. Coupled Thermodynamic-Phase Diagram Assessment of the Rare Earth Oxide-Aluminium Oxide Binary Systems. *J. Alloys Compd.* **1992**, *179*, 259−287.
(53) Barin, I.; Knacke, O.; Kubaschewski, O. *Thermochemical Properties of Inorganic Substances*, 1977; p 825.
(54) Decterov, S. A.; Jung, I. H.; Jak, E.; Kang, Y. B.; Hayes, P.; Pelton, A. D. In *Thermodynamic Modelling of the Al_2O_3-CaO-CoO-CrO-Cr_2O_3-FeO-Fe_2O_3-MgO-MnO-NiO-SiO_2-S System and Applications in Ferrous Process Metallurgy*, VII International Conference on Molten Slags Fluxes and Salts, 2004; pp 839-830.
(55) Berman, R. G.; Brown, T. H.; Greenwood, H. J. *A Thermodynamic Database for Minerals in the System Na_2O-K_2O-CaO-MgO-FeO-Fe_2O_3-Al_2O_3-SiO_2*. Atomic Energy of Canada Limited Technical Report TR-377, 70p, 1985.

https://doi.org/10.1021/acsomega.1c02178
ACS Omega 2021, 6, 22525−22536